Structure, Kinetics, and Thermodynamics of Water and Its Ions at the Interface with Monoclinic ZrO$_2$ Resolved via *Ab Initio* Molecular Dynamics

Jing Yang, Mostafa Youssef, and Bilge Yildiz*

Cite This: https://doi.org/10.1021/acs.jpcc.1c02064

Read Online

ACCESS | Metrics & More | Article Recommendations | SI Supporting Information

ABSTRACT: In this work, we assess the structural, kinetic, and thermodynamic nature of water in contact with the monoclinic ZrO$_2$ ($\bar{1}11$) surface by *ab initio* molecular dynamics calculations. We find that water molecules in the first layer immediately facing the solid surface have a preferred orientation, with one water intramolecular bond, O$_w$–H$_w$, lying parallel to the surface, and the other water hydrogen H$_w$ atom pointing away from the surface. This originates from the electrostatic attraction between surface Zr and water's oxygen, Zr–O$_w$, and from the hydrogen bonding of surface oxygen and water's hydrogen, O$_s$–H$_w$. The short-range interactions between interfacial water and the surface ions of ZrO$_2$ lead to an ordered structure for water molecules, with alternating hydrogen-rich and oxygen-rich layers that persist for more than 5 Å away from the surface. The surface structural perturbation also leads to a shortened hydrogen-bond distance and distorted hydronium ion solvation shell, which leads to faster proton hopping dynamics and lowered solvation free energy of the hydronium ion. By analyzing

these observations in a spatially resolved way, we demonstrate a clear link between the interfacial water structure, localized dynamics, and thermodynamic effects. This work provides an atomistic understanding of the interaction of hydrated protons with the ZrO$_2$ surface in aqueous environment and allows for further engineering of oxide surfaces for targeted hydrogen activity.
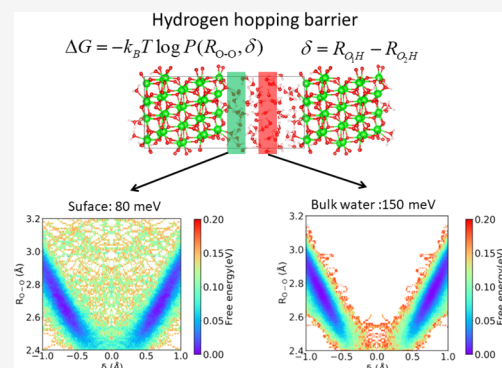
1. INTRODUCTION

Understanding water properties at oxide interfaces is fundamentally important for a wide range of electrochemical applications such as in corrosion,[1−3] photochemical water splitting,[4−7] and heterogeneous catalysis.[8−10] Interfacial water structure is distinct from that of bulk, and the dissociative configurations of water at the oxide surface determine the energetic barrier of various reactions of interest, such as proton incorporation, oxygen evolution reaction, and hydrogen evolution reaction.[11] *Ab initio* molecular dynamics (AIMD) technique has proven to be an effective method for studying water properties, both in bulk[12−14] and at oxide/water interfaces including the oxides CeO$_2$,[15] ZnO,[16] TiO$_2$,[17,18] Fe$_2$O$_3$,[19] MgO,[20] Co$_3$O$_4$,[21] Al$_2$O$_3$,[22] and cubic ZrO$_2$.[23] The immediate first layer of water at the interface is widely studied in these systems. However, the spatially resolved properties need more attention, as water transitions from the bulk-like structure far away from the interface to the disturbed interfacial structure in the immediate vicinity of the oxide surface. This extended interface within water is related to the formation of a mesoscale electric double layer[24] and further influences the interaction between an aqueous electrolyte and the charged defects in an oxide material.[25] A quantitative evaluation of water structure, kinetics, and thermodynamics in such an

extended interfacial zone is needed for a more accurate description of the electrochemical processes therein.

With this goal in mind, in this paper, we present our work on AIMD simulations of monoclinic m-ZrO$_2$/water interface as a model system of technological relevance. Zirconium oxide (or zirconia) is a well-studied oxide material for its application in catalysis, thermal barrier coatings, as a biomaterial, and as a passivation layer on zirconium alloys in corrosion.[26−28] ZrO$_2$/water interface is of particular interest in two scenarios. First, biomedical grade zirconia is prone to aging when attacked by water, which raises questions on whether we should continue to use zirconia in clinical implants.[29,30] This degradation process, which occurs at intermediate temperatures, is referred to as low-temperature degradation (LTD). Understanding the water structure and dynamics on the ZrO$_2$ surface also provides knowledge of LTD kinetics and future engineering of zirconia-based biomaterials. Second, this interface serves as the source of oxidation and hydrogen pickup for zirconium alloys
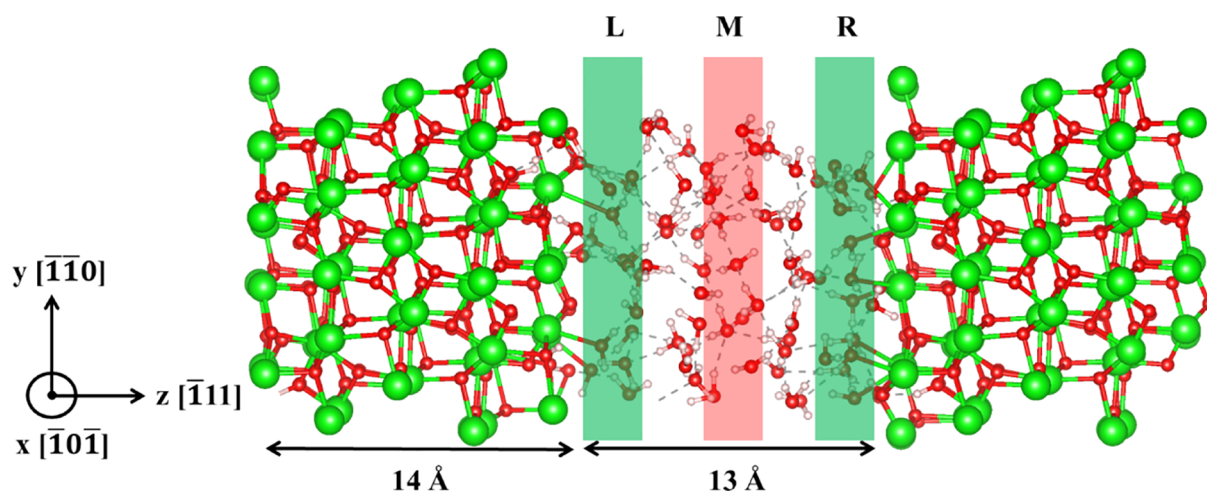
Figure 1. m-ZrO$_2$ ($\bar{1}$11)/water interface as modeled in AIMD simulation. A water film of 13 Å thickness is used. Hydrogen ions are drawn small and white, while oxygen ions medium-sized and red. Zr ions are the largest and green. The three shaded areas in the left (L), middle (M), and right (R) are analyzed separately to show the difference between bulk-like water (region M, red shading) and interfacial water (regions L and R, green shading). The figure is generated with visualization software VESTA.[49]

in nuclear reactors.[31] Zirconium alloy is used for for nuclear fuel cladding and is exposed to high-temperature coolant water (about 500−700 K). As the corrosion onsets, a ZrO$_2$ layer forms and grows on the alloy and passivates Zr against fast corrosion.[32] The cathodic reaction in this process is the reduction of the protons released on the surface. The hydrogen atoms generated in the reduction reaction could either recombine and form hydrogen gas or diffuse through the oxide layer into the zirconium metal. The latter is a detrimental process called hydrogen pickup, leading to the embrittlement of the alloy.[31,33] An atomistic understanding of the ZrO$_2$/water interface is required for resolving the species responsible for the kinetics of oxidation and hydrogen pickup and potential engineering toward better corrosion and hydrogen resistance for zirconium alloy.

We organize the analysis of the AIMD simulations into three parts. First, we present spatially resolved structural information for water and hydronium ion solvation shell. By analyzing the atomic density profile, bond angle distribution, and radial distribution functions, we arrive at a full picture of the interfacial water structure, which has a close-packed hydrogen-bond network and distorted hydronium solvation shell. Second, we quantify the hopping barrier for protons, both in the interfacial zone and in the bulk-like region. We observe a reduction in the barrier by a factor of 2 at the interface, which corresponds to a 10-fold increase in the proton hopping rate at room temperature. This accelerated proton dynamics arises from the strengthening of the hydrogen bond and weakening of the intramolecular bond in the interfacial water layer. Third, we examine the solvation free-energy profile of the hydronium ion as a function of its distance starting from the bulk-like region toward the ZrO$_2$ surface. An adsorption free energy of 0.20 eV is found for the hydronium ion and 0.15 eV for the hydroxide ion at the surface at room temperature. The comprehensive analysis and quantification of the structural, kinetic, and thermodynamic properties in a spatially resolved fashion allow us to establish a clear link between these properties and provide a mechanistic understanding of the proton interaction with the ZrO$_2$ surface.

2. METHODS

AIMD calculations were performed for the ZrO$_2$/water system with Vienna Ab initio Simulation Package (VASP).[34−37] The simulation cell contains 96 formula units of the monoclinic phase ZrO$_2$ with ($\bar{1}$11) surface orientation and 80 water molecules, as shown in Figure 1. The ($\bar{1}$11) surface has been shown to be the surface orientation with the lowest energy.[38] The middle layer of ZrO$_2$ was fixed at the ideal bulk positions to represent the bulk material. Forty configurations with H$^+$ and OH$^-$ ions sitting at different distances toward the ZrO$_2$ surface are set as initial configurations. For the charged cell calculations, a neutralizing background is added, as implemented in VASP. To overcome the timescale limitation of AIMD simulations, each configuration is first equilibrated using classical MD, employing a flexible simple point charge model for water[39] and a Lennard-Jones potential for ZrO$_2$[27] using the GULP code[40,41] for 10 ns in an NPT ensemble with a time step of 0.1 fs and T = 300 K. In the classical MD equilibration process, the positions of ZrO$_2$ atoms are fixed, and only water molecules are allowed to move. The output structures are then modified by adding or extracting one H$^+$ ion at different positions to obtain the initial configurations for AIMD calculations. They are further equilibrated in AIMD employing a velocity-rescaling thermostat for 1 ps, during which the velocities are rescaled every 10 steps. 1 ps run in an NVT ensemble is performed as the production phase for each of the 40 configurations with a Nose−Hoover thermostat. A time step of 0.25 fs and a temperature of 330 K are used throughout the AIMD simulation. In other words, a total of 40 ps production run is used to generate all the structural properties analyzed in this paper.

We have limited this study to the room temperature. 330 K is selected to correct for the known over-binding error of density functional theory (DFT) on bulk water.[42] The temperature-dependent behavior of the water/oxide interface is also a valuable problem that needs to be further explored.

The simulation cell size is 13.6 Å × 13.6 Å × 27.2 Å with a water film thickness of 13 Å. AIMD calculations are performed by sampling the reciprocal space at the gamma point only using the generalized gradient approximation with the Perdew−Burke−Ernzerhof functional.[43,44] An energy cutoff
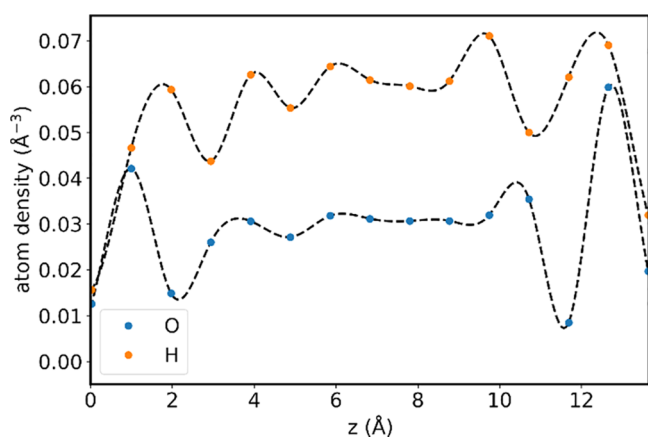
of 400 eV is used. Dispersion corrections are applied using the Grimme D3 method with Becke−Jonson damping.[45,46] Despite the fact that zirconium is a heavy element, it does not contain unpaired d electrons that generally require to be treated with DFT + U.[47] Our previous studies have shown that DFT already gives correct description of the defect energetics in ZrO_2,[31,48] and as such, the Hubbard U term is not included in this work.

For the purpose of comparison, the same simulations are also performed for bulk water of 256 water molecules with no ZrO_2 surface with a density of 0.98 g/cm³. For the bulk water calculation, one configuration is used for neutral, H^+, and OH^- calculations, respectively.

To demonstrate the interfacial effect on the water structure and dynamics, spatially resolved analysis is performed with gridding in the direction perpendicular to the surface. As schematically shown in Figure 1, three regions, left (L), middle (M), and right (R), are selected, with the left and right regions being close to the surface and the middle region away from the surface. In the z direction, the zero position is referenced to the highest oxygen from the ZrO_2 surface in the initial frame in the production run. Each region is 2 Å in thickness. For all the structural and dynamical properties studied in this work, we examine the differences between the three regions to demonstrate the effect of disrupting the water structure with the ZrO_2 surface. It is to be noted that due to the symmetry of the simulation cell, the left and right layers are equivalent and represent the same interfacial region. The middle layer, as we show in the Results and Discussion section, retains the properties of bulk water.

The spatially resolved radial distribution functions are defined such that for each pair of atoms, type A and type B, $g_{AB}(r)$ in some region G counts the distribution of all type B atoms within a distance of r and $r + dr$ away from atom A, with A limited to region G. When r is small, both A and B atoms in the pair are in region G with a high probability. When r is large, the B atom is most likely outside region G. In these analyses, we focus on the radial distribution function variation in a short range in order to see the effect of the surface.

The preferred locations of water molecules are analyzed from density profiles (Figure 2), O−H bond orientation (Figure 3), and radial distribution functions (Figure 4). In other words, it is based purely on the outcome geometry of the AIMD run. The schematic plot in Figure 7 summarizes the most prominent features we obtained from these analyses.

For the postprocessing of the MD trajectories, an ion recognition algorithm is used to automatically detect and dynamically track the hydronium ion H_3O^+ and the hydroxide ion OH^-. Details of the tracking scheme can be found in Section S1 of the Supporting Information.
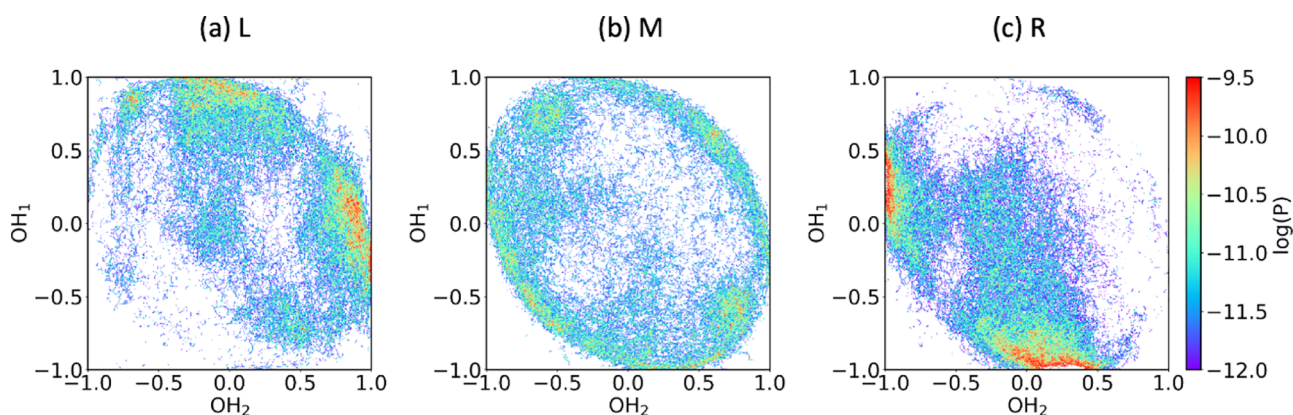
3. RESULTS AND DISCUSSION

In this section, we present the spatially resolved structure and the kinetic and thermodynamic properties of water at the ZrO_2 surface. First, we analyze the structural information provided by AIMD simulations by looking at the atom density profiles, bond angles, and pair correlation functions. In summary, we found strong dissociative adsorption of water molecules, with their hydrogen (H_w) attached to surface oxygen (O_s) and water oxygen (O_w) attached to surface zirconium (Zr_s). Our Bader charge analysis shows that the ZrO_2 surface donates electronic charge to the interfacial water layer, which makes the surface hydroxyl hydrogen a worse hydrogen-bond donor and the surface oxygen a better hydrogen-bond acceptor. This interface effect gives rise to O_w−H_w bond lengths ranging between 1.1 and 1.4 Å, which fall in the gap between the intramolecular O−H bond (<1.0 Å) and intermolecular hydrogen bond (~1.8 Å in bulk water). The increased negative charge of water oxygen also leads to a shortening of hydrogen bonds and increases the compactness of the surface hydrogen-bond network. In the meantime, the intramolecular O_w−H_w bonds are weakened. This structural change is also manifested in the solvation shell of surface hydronium ions, where we observe symmetry breaking of the three hydrogen atoms within the hydronium ion due to surface adsorption. Second, we take a closer look at the proton exchange reaction dynamics. The results show that the proton hopping barrier is reduced by half at the interface, which is clearly linked to the shortened hydrogen bond and the formation of surface hydroxyl groups. Finally, we present the solvation free-energy profiles of the hydronium ion and the hydroxide ion as a function of their distances to the surface and discuss the structural origins of these profiles based on the electrostatic interaction between the ions and the background charge oscillations of interfacial water.

3.1. Structure of Interfacial Water. We start with the thermally equilibrated liquid water structure from classical MD using empirical force field. During the AIMD equilibration, we observe a preferred dissociative adsorption occurring at the interface, which has also been reported previously for a water film on the ZrO_2 surface.[50] In Figure 2, we plot the xy planar-averaged atom density of hydrogen and oxygen on the water side. The density profile clearly exhibits heterogeneity in the z direction, within 3 Å of the ZrO_2 surface. Within the immediate 1 Å thick water layer, the densities of oxygen and hydrogen are approximately the same. In the next 2 Å layer, we see alternating oxygen-rich layers and hydrogen-rich layers, where the maxima of oxygen density meets the minima of hydrogen and vice versa. This alternating feature fully disappears beyond 5 Å away from the ZrO_2 surface, and we see a relatively constant density right in the middle region, with the density of hydrogen being 2 times that of oxygen.

To further understand the local structure of adsorbed water molecules, in Figure 3, we show the joint probability

Figure 2. Planar-averaged atomic density of oxygen and hydrogen as a function of the distance z from the ZrO_2/water interface. The points represent the histogram generated from the original data, and the dashed lines are fitted with spline interpolation. The origin of z coordinate corresponds to the top surface oxygen layer of ZrO_2.

Figure 3. Joint probability distribution, P, of O_w-H_w bond angles with respect to the ZrO_2 surface normal $\mathbf{n}$, plotted in log scale. Here, H_1 and H_2 refer to the two nearest-neighbor hydrogen atoms to water's oxygen. Consider the vector $\mathbf{r}_{OH_i} = \mathbf{r}_{H_i} - \mathbf{r}_O$, where $\mathbf{r}_{H_i}$ and $\mathbf{r}_O$ represent unit vectors in the direction of the position vectors for the corresponding hydrogen and oxygen ions. The coordinates (OH_1, OH_2) of each point in the shown distributions are calculated with the expression $OH_i = \frac{\langle \mathbf{r}_{OH_i}, \mathbf{n} \rangle}{|\mathbf{r}_{OH_i}|}$, where $\langle \mathbf{r}_{OH_i}, \mathbf{n} \rangle$ represents the scalar product of the two vectors, and $|\mathbf{r}_{OH_i}|$ represents the vector length. The case $OH_i = 0$ represents an O_w-H_w pair lying parallel to the ZrO_2 surface, and $OH_i = \pm 1$ represents an O−H pair lying perpendicular to the ZrO_2 surface. L, M, and, R region notations are described in Figure 1.
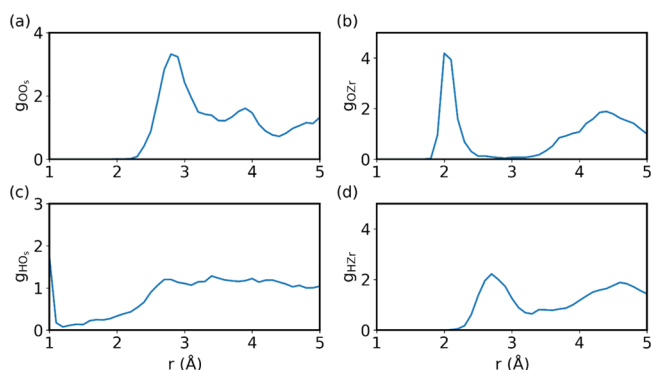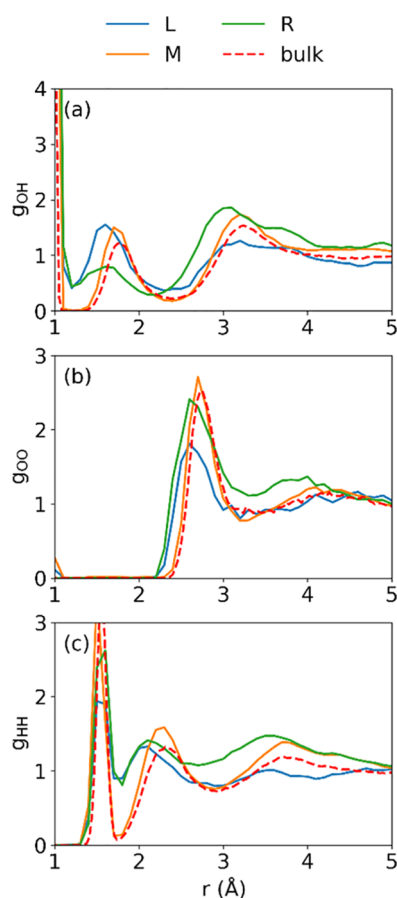

Figure 4. Radial distribution functions of interfacial water molecules in region L with surface zirconium atoms (Zr) and oxygen atoms (O_s).

distribution of the cosines of angles between the two intramolecular O_w-H_w bonds in each water molecule and the ZrO_2 surface normal $\mathbf{n}$. The distribution is spatially resolved in regions L, M, and R defined above. Following the distribution plot, in the middle layer (Figure 3b), the bond angle distribution tends to be isotropic with respect to the surface normal, as expected in bulk water. However, looking at the left and right regions, which are close to the surface, we see a preferred orientation, with one O_w-H_w bond parallel to the surface ($\cos(\theta) = \pm 1$) and the other perpendicular to the surface ($\cos(\theta) = 0$), with hydrogen pointing away from the surface. This preference explains the local density feature shown in Figure 2. In the immediate vicinity of the surface, there exists a layer with O−H pairs lying parallel to the surface, leading to comparable O and H atom densities. The other hydrogen atom, which points away from the surface, contributes to the second layer which is hydrogen-rich.

Figure 4 shows the radial distribution function of the surface atoms of ZrO_2 relative to interfacial water in region L. By comparing the first peak positions of the radial distribution functions of oxygen and hydrogen, we can conclude that hydrogen atoms are attached to surface oxygens O_s, with a sharp peak at ∼ 1 Å (Figure 4c). This peak represents surface hydroxylation, and we observe a 50% dissociative adsorption

rate of surface water molecules, hydroxylating 20% of twofold-coordinated surface oxygens (detailed analysis in Supporting Information Section S2). The first-layer hydrogen forms an O_w-H_w intramolecular bond parallel to the surface. The water oxygen atom sits closer to surface zirconium (2.0 Å) compared to surface oxygen (2.8 Å). This $Zr-O_w$ bond length is comparable to the surface $Zr-O_s$ bond (1.9−2.2 Å). Bader charge analysis[51] (details in Supporting Information Section S3) shows that hydrogen atoms attached to surface oxygens have less positive charge, compared to bulk water hydrogen. Oxygen from water attached to the surface zirconium atoms, on the other hand, shows a more negative charge in comparison to bulk water oxygen. The net effect is that the ZrO_2 surface donates electrons to surface water; thus, a net negative charge is formed in the first interfacial layer and a net positive charge is formed on the ZrO_2 surface.

The change in surface water charge is accompanied by a change in both water and hydronium ion structures, as we detail next. In Figure 5 we take a close look at the radial distribution functions of interfacial water, comparing the three regions (L, M, and R) with bulk results (red dashed line). It is obvious that the middle region retains the structure of bulk water, both in the peak positions and peak heights. Interfacial water, as represented by regions L and R, exhibits the following features which differ from that of bulk water: (1) the second g_{OH} peak distance, which represents an intermolecular hydrogen bond, is shortened by about 0.2 Å. This indicates a strengthened hydrogen bond of interfacial water. The interfacial water oxygens become better hydrogen-bond acceptors due to their bonding with surface zirconium which makes water oxygen more negatively charged. (2) For bulk water, no O−H pair exists in the range of $r_{OH} = 1.1-1.4$ Å, which is a clear separation between the well-defined intramolecular O−H bond and intermolecular hydrogen bond. However, we observe O−H bond lengths within this range in regions L and R. This is a result of the dissociative water adsorption. (3) The first g_{OO} peak and the second g_{HH} peak are also shifted to lower values of r by 0.15 and 0.2 Å, respectively. This observation is a consequence of the shorter hydrogen bonds at the interface, which draw water molecules in the first

Figure 5. Radial distribution functions for bulk water (red dashed line) and water interfacing with ZrO_2 (solid lines).

solvation shell closer to each other, forming a tight hydrogen-bond network.

Knowing the interfacial water structure, in Figure 6 we further analyze the solvation shell of the hydronium ion H_3O^+. The oxygen bonded with excess hydrogen is denoted by O*
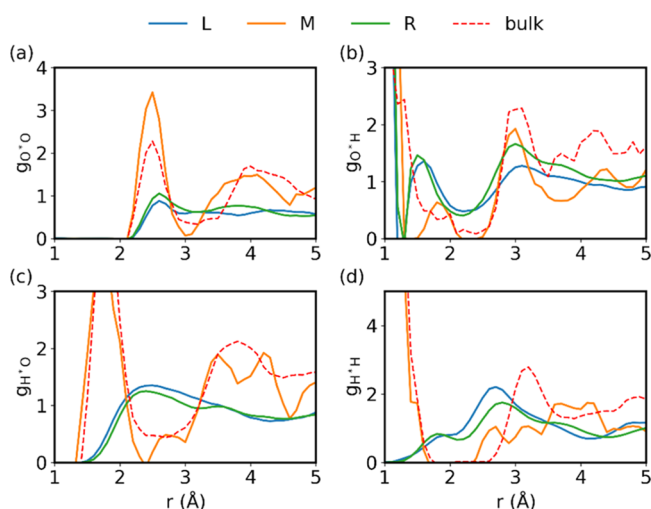
**Figure 6.** Spatially resolved radial distribution functions of hydronium ion: (a) O*−O, (b) O*−H, (c) H*−O, and (d) H*−H. O* represents the oxygen atom that is bonded with the extra proton. H* represents the hydrogen atom that is furthest to O* out of the three hydrogen atoms in H_3O^+.

and the excess hydrogen is denoted by H*. For the hydronium ion in bulk, the three protons are equivalent to a first-order approximation, and all form hydrogen bonds with other H_2O molecules.[12] Due to the positive charge of H_3O^+, the first peak O*O distance (2.5 Å) is shorter than the OO distance in pure water (2.8 Å). In Figure 6a, we see that this first O*O peak is suppressed and slightly lengthened by 0.1 Å in L and R regions, which reverses the trend in the interfacial OO radial distribution (first peak shortened).

By looking at g_{O*H} and g_{H*O} in Figure 6b,c, we observe that for hydronium ion in bulk water, O* differs from O in that it is not a proton acceptor and cannot form hydrogen bond with surrounding hydrogen atoms. The second OH peak at r_{OH} = 1.4−2.2 Å, which represents a hydrogen bond, disappears for O*H in bulk water (and to some extent, it disappears in the M region). Compared to that in bulk water, all the three hydrogens in H_3O^+ bond with O* with a bond length of 0.9−1.5 Å. However, at the interface (L and R regions), as shown in Figure 6b, the peak at 1.5 Å reappears, now representing the bond between O* and H* in the hydronium ion at the interface. This is also reflected in the g_{H*O} plot (Figure 6c), where we see that the first sharp H*O peak at 1.3 Å in bulk water disappears for regions L and R. Overall, this indicates the broken symmetry of H* and the two other hydrogen ions of the hydronium ion in the L and R regions. Because of the bonding between H* and surface oxygen O_s, the O*H* interaction is significantly weakened. H* is driven further away from O* (Figure 6b,c), and subsequently, driven away from the other hydrogen atoms within the hydronium ion (Figure 6d). Another way to look at the lengthened H*−O* distance is that, H* forms a hydroxyl group with surface oxygen, breaking the hydronium ion into a water molecule and a O_s−H hydroxyl group.

As a concise presentation for all structural effects of the ZrO_2 surface on interfacial water presented in this section, we summarize the atomic structure and bond length information schematically in Figure 7. We observe that due to the surface Zr−O_w and O_s−H_w bonding, geometrically, an adsorbed water molecule is flattened by the surface, with one O_w−H_w bond
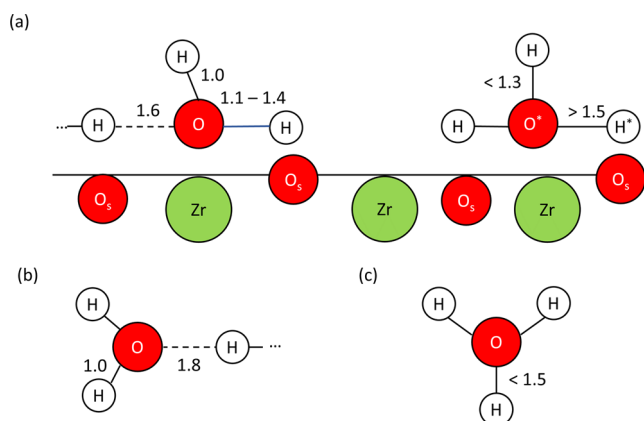
Figure 7. Schematic plot for atomic configurations and bond lengths for (a) water molecule and a hydronium ion at the ZrO_2 surface, (b) water molecule in bulk water, and (c) hydronium ion in bulk water. Hydrogen bonds are presented by black dashed lines. Black solid lines represent intramolecular bonds. In (a), we see O−H bond length between 1.1 and 1.4 Å on the surface, which can be either a weak intramolecular bond or a strong hydrogen bond and as such is represented by a blue solid line.
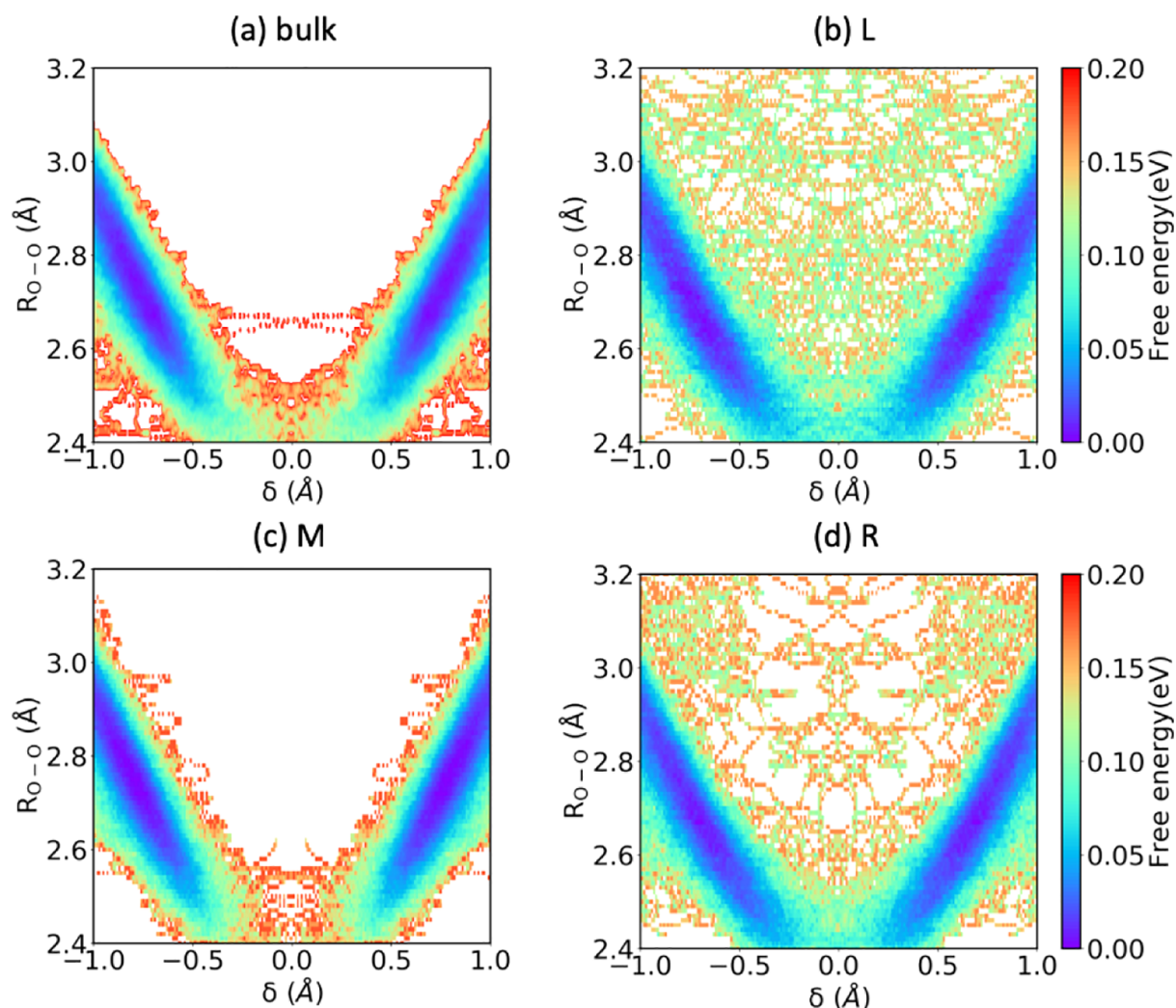
Figure 8. Calculated free-energy landscapes of the proton hopping process between two water oxygens O_w (a) in bulk water and (b−d) in L, M, and R regions at the ZrO_2/water interface. For each region, the zero point of free energy is referenced to the minimum value within the region. White-colored regions represent configurations that have zero probability.

lying parallel to the surface. This bonding orientation preference at the interface also leads to alternating hydrogen-rich and oxygen-rich layers deep into water. Meanwhile, Zr−O_w bonding increases the negative charge of water's oxygen, shortening the hydrogen bond length between oxygen in water molecules and the neighboring hydrogen donors. Surface dissociative adsorption gives rise to O_w−H_w bond lengths between 1.1 and 1.4 Å, which belong to the blurred transition zone between a weak intramolecular covalent bond and a strong intermolecular hydrogen bond. This O_w−H_w bond length is forbidden in bulk water (Figure 5a) but arises as an intermediate state in the surface hydrogen hopping process.[15] In the case of the hydronium ion, adsorption at the water/ zirconia interface breaks the symmetry of the three hydrogen atoms. H* is strongly bonded to surface oxygen, and thus the bond length of O*−H* is observably longer than the bonds between O* and the other two hydrogen atoms. In cases where the O*−H* distance is large enough, we can say that the hydronium ion has broken into a water molecule and a surface hydroxyl group. However, due to the increased negative charge of O* at the interface, the interfacial hydronium ion overall forms stronger intramolecular bonds compared to the bulk

hydronium ion. The distinct interfacial water structure changes its dynamics drastically, as will be discussed in Section 3.2.

3.2. Proton Dynamics at the ZrO_2/Water Interface. In this section, we quantitatively demonstrate the surface effect on proton-transfer dynamics by calculating the free-energy landscapes of proton hopping between two water oxygen atoms at different distances toward the ZrO_2 surface. By identifying the two nearest-neighbor water oxygen atoms O_1 and O_2 for one hydrogen atom H, we can define the proton hopping reaction coordinate $\delta = R_{O_1-H} - R_{O_2-H}$, where R_{O_1-H} and R_{O_2-H} are the distances between O_1 and O_2 to H, respectively. $\delta = 0$ represents that the hydrogen atom is equally shared by the two oxygen atoms, that is, in the middle of the proton hopping process. We construct a two-dimensional free-energy landscape of the proton hopping reaction by calculating $\Delta G = -k_B T \log P(R_{O-O}, \delta)$, where P is the probability distribution of the configuration of the O_1−H−O_2 triplet with respect to δ and oxygen−oxygen distance R_{O-O}. The resultant free-energy maps can provide both the energetics and atomic configurations of the proton hopping process.

Comparison of proton hopping free-energy landscapes in regions L, M, and R and in bulk water is shown in Figure 8. We

observe that the energy map in the middle region is both qualitatively and quantitatively very similar to that in bulk water. The free-energy minimum is located within the R_{O-O} range of 2.7−2.8 Å, which is consistent with the first g_{OO} peak, as shown in Figure 5b. We can also say that for the proton exchange reaction to happen in bulk water, the distance between O_1 and O_2 should be below 2.6 Å. The minimum energy path yields a hopping barrier of about 150 meV in bulk as well as in region M, which is consistent with previous studies.[15,16]

Now, we look at regions L and R, which are significantly influenced by the interface effect. The saddle point of the free-energy landscape ($\delta = 0$, R_{O-O} 2.4−2.5 Å) is notably lowered at the interface. The hopping barrier is reduced to about 80 meV, which corresponds to a 10 times faster reaction rate at room temperature. This value is compared to the short-range hopping barriers of 100 meV found on the ZnO surface and on the CeO$_2$-supported Pt clusters.[15] We also observe that there is a large area in the middle of the energy map (δ −0.25−0.25 Å, R_{O-O} > 2.6 Å), which previously had zero probability in bulk and now becomes a possible proton hopping route. This observation is a direct result of hydrogen bonding to surface oxygen O$_s$ and the weakened intramolecular O$_w$−H$_w$ bond. This is also confirmed in Figure 9, where we show the same
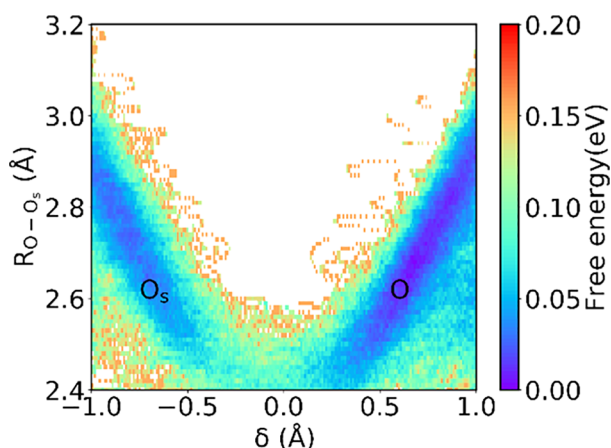

Figure 9. Calculated free-energy landscape of proton hopping between surface oxygen (O$_s$) and water oxygen (O).

free-energy landscape of proton hopping between surface oxygen O$_s$ and oxygen in water. Here, the shape of the probability distribution is closer to that in bulk, where the O$_s$−O distance has to be under 2.6 Å for the exchange reaction to happen. This surface oxygen-assisted hopping process allows for more flexible O−O configuration and also shows a low barrier of about 80 meV.

From the above analysis, we can conclude that proton hopping takes place about 10 times faster in the interfacial zone, and this arises from the structural effect of the interface described in Section 3.1. First, interfacial water structure features a more close-packed hydrogen-bond network due to the increased strength of the intermolecular hydrogen bond for interfacial water at the expense of the intramolecular O−H bond. Thus, hydrogen from a proton donor is more likely to hop toward the oxygen to which it is hydrogen-bonded. This leads to the lowered hopping barrier in regions L and R representing interfacial water. Second, we have shown that hydrogen in the first layer in the vicinity of the ZrO$_2$ surface is

strongly bonded with surface oxygen. This allows for the surface-assisted hopping mechanism presented in Figure 9, as the dissociatively adsorbed hydrogen hops between surface oxygen and water oxygen.

3.3. Thermodynamics of Hydronium and Hydroxyl Ion Adsorption at the ZrO$_2$/Water Interface.

In this section, we investigate the thermodynamics of hydronium ion and hydroxide ion adsorption at the ZrO$_2$/water interface by sampling their probability distribution P as a function of z. Following the same free-energy formation $\Delta G = -k_B T \log P(z)$, we can obtain the relative adsorption free-energy profiles at different positions toward the ZrO$_2$ surface for both ions, as shown in Figure 10. Both curves display symmetric features as
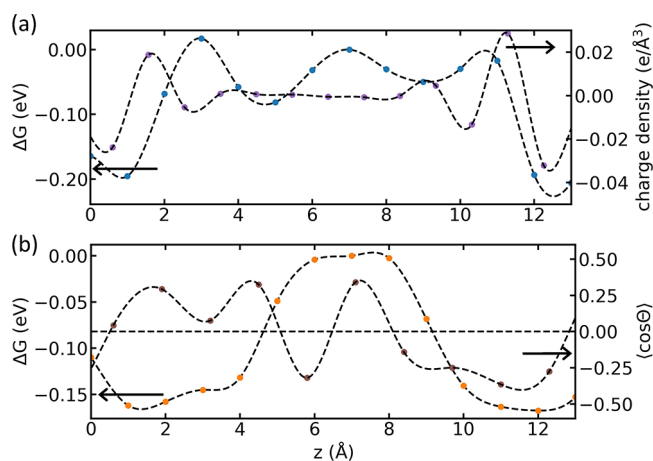
Figure 10. (a) Adsorption-relative free-energy profiles of H$_3$O$^+$ ion (blue dotted line) and local charge density (purple dotted line) as a function of z. The charge density is calculated by adding up the averaged Bader charge (−1.270 for O$_w$ and +0.635 for H) multiplied by atom density. (b) Adsorption free-energy profile of OH$^-$ ion (yellow dotted line) and the averaged cosine of the angle θ between the O−H bond and the ZrO$_2$ surface normal (brown dotted line) as a function of z. θ is defined by $\cos\theta = \frac{\langle r_{OH}, \, n \rangle}{|r_{OH}||n|}$, where n is the surface normal pointing in the direction of increasing z. Because of this definition of surface normal, there is asymmetry in the $\langle \cos\theta \rangle$ profile between the left and right interfaces.

required by the equivalence of the two surfaces in the simulation cell, which is an evidence of sufficient sampling. We observe that the hydronium ion profile exhibits a minimum, followed by a maximum within 3 Å in the vicinity of the surface, followed by another energy minimum at about 5 Å. Similar behavior has been shown previously for metal ions approaching a calcite surface.[52] It mainly results from the electrostatic interaction between the positively charged ion and the water structure forming the solvation shell. The first energy minimum originates from the distorted solvation shell of the hydronium ion close to the surface. In the interfacial zone where the hydrogen network is more compact, the distinction between the covalent O$_w$−H$_w$ bond and hydrogen bond is blurred and the barrier for oxygen to obtain an excess proton is lowered. The second energy minimum originates from the electrostatic potential built up by the alternating hydrogen-rich (positively charged) and oxygen-rich (negatively charged) water layers, as the charge density profile in Figure 10a shows. Due to the alternating nature of the density profile close to the surface, $\Delta G(H_3O^+)$ profile also displays multiple minima and maxima. In other words, next to a negative charge minimum, a

positive charge maximum arises. The location of this positive maximum favors the presence of the hydronium ion, which manifests itself as reduction in the relative free energy of adsorption.

For hydroxide ions, we observe a relatively wide free-energy well within 5 Å of the surface. The widening of the free-energy well indicates that the point charge model for hydronium ion (or proton) and metal ions does not apply to hydroxide ions. Due to its diatomic structure, its electrostatic interaction with the background water molecule solvent is more complex. By analyzing the O−H bond direction in Figure 10b, we see that in the range of 1−4 Å, next to the zirconia surface, there is a tendency of O−H to point away from the surface. This correlates with the width of the adsorption free-energy well shown in the same figure.

We observe that there exists a thermodynamic well of 0.2 eV for hydronium ions to be trapped within 1−2 Å from the ZrO_2 surface, which coincides with the length scale of the Stern layer of the electric double-layer theory.[53] Combining the thermodynamic profile with the density information, we can conclude that the Stern layer crowded with excess proton is expected at the ZrO_2/water interface. Such quantification allows for further numerical modeling of hydrogen evolution reaction at the surface and hydrogen entering zirconium oxide.

4. CONCLUSIONS

In this paper, we quantitatively assessed the structural, kinetic, and thermodynamic effects of the ZrO_2 surface on water via *ab initio* MD calculations. The spatially resolved analysis clearly reveals links between the hydrogen-bond network, proton hopping dynamics, and adsorption thermodynamics. We have shown that interfacial water has a more close-packed hydrogen-bond network compared to bulk water and displays an ordered structure with alternating hydrogen-rich and oxygen-rich layers within 5 Å from the surface. This is due to both covalent and hydrogen bonding between water's hydrogen and oxygen on the zirconia surface (O_s) and also due to iono-covalent bonding between water's oxygen (O_w) and Zr. This close-packing is accompanied by shortened and stronger hydrogen bonds and longer and weaker covalent bonds among the water species at the interface. This structural distortion lowers the barrier of the proton exchange reaction by half and allows for surface-assisted proton hopping to happen. Adsorption free-energy profiles of hydronium ions also indicate a connection between the structural effects and thermodynamic properties, giving adsorption free energy of 0.20 eV for the hydronium ion and 0.15 eV for the hydroxyl ion. The results here provide a mechanistic and quantitative understanding of the proton and hydroxyl group dynamics and thermodynamics at the ZrO_2/interface, which could guide further engineering of oxide surfaces toward desired water/oxide interactions. Specifically, we identify electron transfer from ZrO_2 to interfacial water as an important mechanism that enhances surface proton hopping. In applications where hydrogen transport is undesirable, such as nuclear cladding and biomedical coating, surface modifications that impede the charge-transfer process would be valid approaches to prevent material degradation. The opposite is true, that is, by promoting surface charge transfer, one also promotes hydrogen transport at the surface, which can be beneficial in heterogeneous catalytic processes such as oxygen evolution reaction.

■ ASSOCIATED CONTENT

ⓈI Supporting Information

The Supporting Information is available free of charge at https://pubs.acs.org/doi/10.1021/acs.jpcc.1c02064.

Automatic recognition algorithm of hydronium and hydroxyl ions; surface hydroxylation and water dissociation; and Bader charge analysis for surface oxygen and hydrogen atoms (PDF)

■ AUTHOR INFORMATION

Corresponding Author

Bilge Yildiz − *Laboratory for Electrochemical Interfaces, Department of Materials Science and Engineering, Massachusetts Institute of Technology, Cambridge, Massachusetts 02139, United States; Department of Nuclear Science and Engineering, Massachusetts Institute of Technology, Cambridge, Massachusetts 02139, United States;* ⓞ orcid.org/0000-0002-2688-5666; Email: byildiz@mit.edu

Authors

Jing Yang − *Laboratory for Electrochemical Interfaces, Department of Materials Science and Engineering, Massachusetts Institute of Technology, Cambridge, Massachusetts 02139, United States;* ⓞ orcid.org/0000-0003-1855-0708

Mostafa Youssef − *Laboratory for Electrochemical Interfaces, Department of Materials Science and Engineering, Massachusetts Institute of Technology, Cambridge, Massachusetts 02139, United States; Department of Nuclear Science and Engineering, Massachusetts Institute of Technology, Cambridge, Massachusetts 02139, United States; Department of Mechanical Engineering, The American University in Cairo, New Cairo 11835, Egypt;* ⓞ orcid.org/0000-0001-8966-4169

Complete contact information is available at:
https://pubs.acs.org/10.1021/acs.jpcc.1c02064

Notes

The authors declare no competing financial interest.

■ REFERENCES

(1) Motta, A. T.; Couet, A.; Comstock, R. J. Corrosion of Zirconium Alloys Used for Nuclear Fuel Cladding. *Annu. Rev. Mater. Res.* **2015**, *45*, 311−343.

(2) Cox, B. Some thoughts on the mechanisms of in-reactor corrosion of zirconium alloys. *J. Nucl. Mater.* **2005**, *336*, 331−368.

(3) Aryanfar, A.; Thomas, J.; Van der Ven, A.; Xu, D.; Youssef, M.; Yang, J.; Yildiz, B.; Marian, J. Integrated Computational Modeling of Water Side Corrosion in Zirconium Metal Clad Under Nominal LWR Operating Conditions. *JOM* **2016**, *68*, 2900−2911.

(4) Scheuermann, A. G.; Lawrence, J. P.; Kemp, K. W.; Ito, T.; Walsh, A.; Chidsey, C. E. D.; Hurley, P. K.; McIntyre, P. C. Design

principles for maximizing photovoltage in metal-oxide-protected water-splitting photoanodes. *Nat. Mater.* **2015**, *15*, 99.

(5) Pham, T. A.; Ping, Y.; Galli, G. Modelling heterogeneous interfaces for solar water splitting. *Nat. Mater.* **2017**, *16*, 401.

(6) Zandi, O.; Hamann, T. W. Enhanced Water Splitting Efficiency Through Selective Surface State Removal. *J. Phys. Chem. Lett.* **2014**, *5*, 1522−1526.

(7) Hussain, H.; Tocci, G.; Woolcot, T.; Torrelles, X.; Pang, C. L.; Humphrey, D. S.; Yim, C. M.; Grinter, D. C.; Cabailh, G.; Bikondoa, O.; et al. Structure of a model TiO₂ photocatalytic interface. *Nat. Mater.* **2016**, *16*, 461.

(8) Indra, A.; Menezes, P. W.; Driess, M. Uncovering Structure-Activity Relationships in Manganese-Oxide-Based Heterogeneous Catalysts for Efficient Water Oxidation. *ChemSusChem* **2015**, *8*, 776−785.

(9) Aranifard, S.; Ammal, S. C.; Heyden, A. On the importance of metal−oxide interface sites for the water−gas shift reaction over Pt/CeO₂ catalysts. *J. Catal.* **2014**, *309*, 314−324.

(10) Najafpour, M. M.; Renger, G.; Hołyńska, M.; Moghaddam, A. N.; Aro, E.-M.; Carpentier, R.; Nishihara, H.; Eaton-Rye, J. J.; Shen, J.-R.; Allakhverdiev, S. I. Manganese Compounds as Water-Oxidizing Catalysts: From the Natural Water-Oxidizing Complex to Nanosized Manganese Oxide Structures. *Chem. Rev.* **2016**, *116*, 2886−2936.

(11) Mu, R.; Zhao, Z.-j.; Dohnálek, Z.; Gong, J. Structural motifs of water on metal oxide surfaces. *Chem. Soc. Rev.* **2017**, *46*, 1785−1806.

(12) Tuckerman, M.; Laasonen, K.; Sprik, M.; Parrinello, M. Ab initio molecular dynamics simulation of the solvation and transport of hydronium and hydroxyl ions in water. *J. Chem. Phys.* **1995**, *103*, 150−161.

(13) Marx, D.; Tuckerman, M. E.; Hutter, J.; Parrinello, M. The nature of the hydrated excess proton in water. *Nature* **1999**, *397*, 601.

(14) Tuckerman, M. E.; Marx, D.; Parrinello, M. The nature and transport mechanism of hydrated hydroxide ions in aqueous solution. *Nature* **2002**, *417*, 925.

(15) Farnesi Camellone, M.; Negreiros Ribeiro, F.; Szabová, L.; Tateyama, Y.; Fabris, S. Catalytic Proton Dynamics at the Water/Solid Interface of Ceria-Supported Pt Clusters. *J. Am. Chem. Soc.* **2016**, *138*, 11560−11567.

(16) Tocci, G.; Michaelides, A. Solvent-Induced Proton Hopping at a Water-Oxide Interface. *J. Phys. Chem. Lett.* **2014**, *5*, 474−480.

(17) Wang, Z.-T.; Wang, Y.-G.; Mu, R.; Yoon, Y.; Dahal, A.; Schenter, G. K.; Glezakou, V.-A.; Rousseau, R.; Lyubinetsky, I.; Dohnálek, Z. Probing equilibrium of molecular and deprotonated water on TiO₂ (110). *Proc. Natl. Acad. Sci. U.S.A.* **2017**, *114*, 1801−1805.

(18) Calegari Andrade, M. F.; Ko, H.-Y.; Car, R.; Selloni, A. Structure, Polarization, and Sum Frequency Generation Spectrum of Interfacial Water on Anatase TiO₂. *J. Phys. Chem. Lett.* **2018**, *9*, 6716−6721.

(19) McBriarty, M. E.; von Rudorff, G. F.; Stubbs, J. E.; Eng, P. J.; Blumberger, J.; Rosso, K. M. Dynamic Stabilization of Metal Oxide-Water Interfaces. *J. Am. Chem. Soc.* **2017**, *139*, 2581−2584.

(20) Laporte, S.; Finocchi, F.; Paulatto, L.; Blanchard, M.; Balan, E.; Guyot, F.; Saitta, A. M. Strong electric fields at a prototypical oxide/water interface probed by ab initio molecular dynamics: MgO(001). *Phys. Chem. Chem. Phys.* **2015**, *17*, 20382−20390.

(21) Creazzo, F.; Galimberti, D. R.; Pezzotti, S.; Gaigeot, M.-P. DFT-MD of the (110)-Co3O4 cobalt oxide semiconductor in contact with liquid water, preliminary chemical and physical insights into the electrochemical environment. *J. Chem. Phys.* **2019**, *150*, 041721.

(22) Harmon, K. J.; Letchworth-Weaver, K.; Gaiduk, A. P.; Giberti, F.; Gygi, F.; Chan, M. K. Y.; Fenter, P.; Galli, G. Validating first-principles molecular dynamics calculations of oxide/water interfaces with x-ray reflectivity data. *Phys. Rev. Mater.* **2020**, *4*, 113805.

(23) Sato, R.; Ohkuma, S.; Shibuta, Y.; Shimojo, F.; Yamaguchi, S. Proton Migration on Hydrated Surface of Cubic ZrO₂: Ab initio Molecular Dynamics Simulation. *J. Phys. Chem. C* **2015**, *119*, 28925−28933.

(24) Fawcett, W. R. *Liquids, Solutions, and Interfaces: From Classical Macroscopic Descriptions to Modern Microscopic Details*; Oxford University Press: USA, 2004.

(25) Todorova, M.; Neugebauer, J. Extending the Concept of Defect Chemistry from Semiconductor Physics to Electrochemistry. *Phys. Rev. Appl.* **2014**, *1*, 014001.

(26) Chevalier, J.; Gremillard, L.; Virkar, A. V.; Clarke, D. R. The Tetragonal-Monoclinic Transformation in Zirconia: Lessons Learned and Future Trends. *J. Am. Ceram. Soc.* **2009**, *92*, 1901−1920.

(27) Martins, L. R.; Skaf, M. S.; Ladanyi, B. M. Solvation Dynamics at the Water/Zirconia Interface: Molecular Dynamics Simulations. *J. Phys. Chem. B* **2004**, *108*, 19687−19697.

(28) Youssef, M.; Yildiz, B. Intrinsic point-defect equilibria in tetragonal ZrO₂: Density functional theory analysis with finite-temperature effects. *Phys. Rev. B: Condens. Matter Mater. Phys.* **2012**, *86*, 144109.

(29) Chevalier, J. What future for zirconia as a biomaterial? *Biomaterials* **2006**, *27*, 535−543.

(30) Gautam, C.; Joyner, J.; Gautam, A.; Rao, J.; Vajtai, R. Zirconia based dental ceramics: structure, mechanical properties, biocompatibility and applications. *Dalton Trans.* **2016**, *45*, 19194−19215.

(31) Youssef, M.; Yang, M.; Yildiz, B. Doping in the Valley of Hydrogen Solubility: A Route to Designing Hydrogen-Resistant Zirconium Alloys. *Phys. Rev. Appl.* **2016**, *5*, 014008.

(32) Wang, P.; Was, G. S. Oxidation of Zircaloy-4 during in situ proton irradiation and corrosion in PWR primary water. *J. Mater. Res.* **2015**, *30*, 1335−1348.

(33) Suman, S.; Khan, M. K.; Pathak, M.; Singh, R. N.; Chakravartty, J. K. Hydrogen in Zircaloy: Mechanism and its impacts. *Int. J. Hydrogen Energy* **2015**, *40*, 5976−5994.

(34) Kresse, G.; Hafner, J. Ab initiomolecular dynamics for liquid metals. *Phys. Rev. B: Condens. Matter Mater. Phys.* **1993**, *47*, 558−561.

(35) Kresse, G.; Hafner, J. Ab initiomolecular-dynamics simulation of the liquid-metal-amorphous-semiconductor transition in germanium. *Phys. Rev. B: Condens. Matter Mater. Phys.* **1994**, *49*, 14251−14269.

(36) Kresse, G.; Furthmüller, J. Efficiency of ab-initio total energy calculations for metals and semiconductors using a plane-wave basis set. *Comput. Mater. Sci.* **1996**, *6*, 15−50.

(37) Kresse, G.; Furthmüller, J. Efficient iterative schemes forab initiototal-energy calculations using a plane-wave basis set. *Phys. Rev. B: Condens. Matter Mater. Phys.* **1996**, *54*, 11169−11186.

(38) Christensen, A.; Carter, E. A. First-principles study of the surfaces of zirconia. *Phys. Rev. B: Condens. Matter Mater. Phys.* **1998**, *58*, 8050−8064.

(39) Teleman, O.; Jönsson, B.; Engström, S. A molecular dynamics simulation of a water model with intramolecular degrees of freedom. *Mol. Phys.* **1987**, *60*, 193−203.

(40) Gale, J. D. GULP: A computer program for the symmetry-adapted simulation of solids. *J. Chem. Soc., Faraday Trans.* **1997**, *93*, 629−637.

(41) Gale, J. D.; Rohl, A. L. The General Utility Lattice Program (GULP). *Mol. Simul.* **2003**, *29*, 291−341.

(42) VandeVondele, J.; Mohamed, F.; Krack, M.; Hutter, J.; Sprik, M.; Parrinello, M. The influence of temperature and density functional models in ab initio molecular dynamics simulation of liquid water. *J. Chem. Phys.* **2005**, *122*, 14515.

(43) Perdew, J. P.; Burke, K.; Ernzerhof, M. Generalized Gradient Approximation Made Simple. *Phys. Rev. Lett.* **1996**, *77*, 3865−3868.

(44) Perdew, J. P.; Burke, K.; Ernzerhof, M. Generalized Gradient Approximation Made Simple [Phys. Rev. Lett. 77, 3865 (1996)]. *Phys. Rev. Lett.* **1997**, *78*, 1396.

(45) Grimme, S.; Antony, J.; Ehrlich, S.; Krieg, H. A consistent and accurate ab initio parametrization of density functional dispersion correction (DFT-D) for the 94 elements H-Pu. *J. Chem. Phys.* **2010**, *132*, 154104.

(46) Grimme, S.; Ehrlich, S.; Goerigk, L. Effect of the damping function in dispersion corrected density functional theory. *J. Comput. Chem.* **2011**, *32*, 1456−1465.

(47) Anisimov, V. I.; Zaanen, J.; Andersen, O. K. Band theory and Mott insulators: HubbardUinstead of Stoner. *Phys. Rev. B: Condens. Matter Mater. Phys.* **1991**, *44*, 943−954.

(48) Yang, J.; Youssef, M.; Yildiz, B. Oxygen self-diffusion mechanisms in monoclinic ZrO_2 revealed and quantified by density functional theory, random walk analysis, and kinetic Monte Carlo calculations. *Phys. Rev. B* **2018**, *97*, 024114.

(49) Momma, K.; Izumi, F. VESTA 3for three-dimensional visualization of crystal, volumetric and morphology data. *J. Appl. Crystallogr.* **2011**, *44*, 1272−1276.

(50) Korhonen, S. T.; Calatayud, M.; Krause, A. O. I. Stability of Hydroxylated (1−11) and (1−01) Surfaces of Monoclinic Zirconia: A Combined Study by DFT and Infrared Spectroscopy. *J. Phys. Chem. C* **2008**, *112*, 6469−6476.

(51) Tang, W.; Sanville, E.; Henkelman, G. A grid-based Bader analysis algorithm without lattice bias. *J. Phys.: Condens. Matter* **2009**, *21*, 084204.

(52) Kerisit, S.; Parker, S. C. Free Energy of Adsorption of Water and Metal Ions on the {101−4} Calcite Surface. *J. Am. Chem. Soc.* **2004**, *126*, 10152−10161.

(53) Burt, R.; Birkett, G.; Zhao, X. S. A review of molecular modelling of electric double layer capacitors. *Phys. Chem. Chem. Phys.* **2014**, *16*, 6519−6538.